

Basins of Attraction for Chimera States

Erik A. Martens^{a,b,*}, Mark J. Panaggio^{c,d}, and Daniel M. Abrams^{d,e,f}

^a*Dept. of Biomedical Sciences, University of Copenhagen, Blegdamsvej 3,*

2200 Copenhagen, Denmark ^b*Dept. of Mathematical Sciences,*

University of Copenhagen, Universitetsparken 5,

2200 Copenhagen, Denmark ^c*Mathematics Dept.,*

Rose-Hulman Institute of Technology, Terre Haute,

IN ^d*Dept. of Engineering Sciences and Applied Mathematics, Northwestern University,*

Evanston, IL ^e*Dept. of Physics and Astronomy, Northwestern University, Evanston,*

IL ^f*Northwestern Institute on Complex Systems, Northwestern University, Evanston, IL*

Chimera states—curious symmetry-broken states in systems of identical coupled oscillators—occur only for special initial conditions. Here we analyze their basins of attraction in a simple system comprised of two populations. Using perturbative analysis and numerical simulation we evaluate asymptotic states and associated destination maps, and demonstrate that basins form a complex twisting structure in phase space. Understanding the basins’ precise nature may help in development of control methods to switch between chimera patterns, with possible technological and neural system applications.

Self-emergent synchronization is a key process in networks of coupled oscillators, and is observed in a remarkable range of systems, including pendulum clocks, pedestrian’s on a bridge locking their gait, Josephson junctions, flashing fireflies, the beating of the heart, circadian clocks in the brain, chemical oscillations, metabolic oscillations in yeast, life cycles of phytoplankton, and genetic oscillators [1]. About a decade ago, a study [2] revealed the existence of chimera states, in which a population of identical coupled oscillators splits up into two parts, one synchronous and the other incoherent. This state is counter-intuitive as it appears despite the oscillators being identical. Recent experiments using metronomes, (electro-) chemical oscillators and lasing systems [2–5] have demonstrated the existence of chimera states in real-world settings; previous theoretical studies have also confirmed the robustness of chimeras subjected to a range of adverse conditions, including additive noise, varied oscillator frequencies, varied coupling topologies, and other imperfections [6].

Chimeras are known to arise in systems with nonlocal coupling that decays with increasing distance between phase oscillators, thus bridging the gap between the extremes of local (nearest-neighbor) and global (all-to-all) coupling¹. Such long-range coupling is characteristic of many real-world technological [9] and

* erik.martens@ds.mpg.de

¹ For oscillators with non-constant amplitudes it appears that local and global coupling can both be sufficient [7, 8].

biological [10] systems. Chimeras states are solutions stably coexisting with the fully synchronized state, not emerging via spontaneous symmetry breaking, and are thus only attained via a certain class of initial conditions [2, 6]. Figure 1 graphically demonstrates this puzzling aspect of basins of attraction for chimera states: apparently similar initial conditions (panel B) can evolve to completely different steady-states (panel C). Thus, a natural question arising in any practical situation is: given a random initial phase configuration, how likely is the system to converge to a chimera state? Even though this important question was raised in 2010 [11], basins of attraction for chimera states have not yet been investigated systematically.

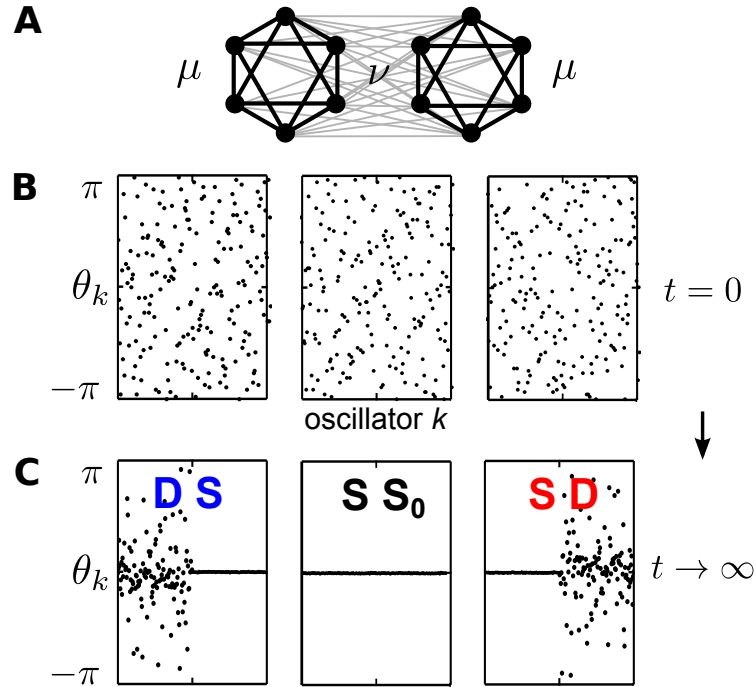


Figure 1. **A:** schematic of the system under investigation. **B:** Three superficially similar oscillator phase distributions taken as initial conditions. **C:** Oscillator phase distributions after long-time evolution of system—each corresponds to the initial condition shown directly above it. Left: “DS” or “desync-sync” state; Middle: “SS₀” or “sync-sync” state; Right: “SD” or “sync-desync” state.

One difficulty with the examination of basins of attractions is that they are computationally expensive to obtain, e.g. via Monte Carlo integration [12]. In this Letter, in contrast, we use primarily analytic methods to explain the structure of the phase space and provide a systematic study of the basins of attraction leading to chimera states in the thermodynamic limit.

Model. The simplest realization of nonlocal coupling is achieved with two populations, where each population is more strongly coupled to itself than to the neighboring population (see Figure 1 panel A). It has been used as a model for several investigations of chimera states [2, 6, 13]; here chimeras manifest themselves as a state with one synchronous and one asynchronous population. Accordingly, we consider

the Kuramoto-Sakaguchi model with $n = 2$ populations [13] each of size N^σ ,

$$\dot{\theta}_k^\sigma = \omega + \sum_{\sigma'=1}^2 \frac{K_{\sigma\sigma'}}{N^{\sigma'}} \sum_{l=1}^{N^{\sigma'}} \sin(\theta_l^{\sigma'} - \theta_k^\sigma - \alpha), \quad (1)$$

where θ_k^σ is the phase of the k th oscillator $k = 1, \dots, N^\sigma$ in population $\sigma \in \{1, 2\}$ and ω is the oscillator frequency. For consistency with previous work [13], we assume the coupling is symmetric with neighbor-coupling $K_{\sigma\sigma'} = K_{\sigma'\sigma} = \nu$ and self-coupling $K_{\sigma\sigma} = \mu$. Imposing without loss of generality $\mu + \nu = 1$, the coupling can be parameterized by the coupling disparity $A = \mu - \nu$. We redefine the phase lag parameter via $\beta = \pi/2 - \alpha$ as chimeras emerge in the limit of near-cosine-coupling ($\beta \rightarrow 0$) for this type of system [13]. The mean field order parameter $R_\sigma e^{i\Phi_\sigma} = N^{-1} \sum_{j=1}^N \exp(i\theta_j^\sigma)$ describes the synchronization level of population σ with $R_\sigma = 1$ for perfect and $R_\sigma \leq 1$ for partial synchronization. We consider the thermodynamic limit $N^\sigma \rightarrow \infty$, allowing us to express the ensemble dynamics in terms of the continuous oscillator density $f^\sigma(\theta, \omega)$. This facilitates a low-dimensional description of the dynamics via the Ott-Antonsen ansatz [14] in terms of the mean-field order parameter of each population, $\rho_\sigma(t) e^{i\phi_\sigma(t)} = \int e^{i\theta} f^\sigma(\theta, t) d\theta$ with $0 < \rho_\sigma \leq 1$ [15].

By virtue of the translational symmetry $\phi_\sigma \rightarrow \phi_\sigma + \text{const.}$, the resulting dynamics are effectively three dimensional with the angular phase difference $\psi = \phi_1 - \phi_2$, obeying

$$\dot{\rho}_1 = \frac{1 - \rho_1^2}{2} [\mu\rho_1 \sin \beta + \nu\rho_2 \sin(\beta - \psi)] \quad (2)$$

$$\dot{\rho}_2 = \frac{1 - \rho_2^2}{2} [\mu\rho_2 \sin \beta + \nu\rho_1 \sin(\beta + \psi)] \quad (3)$$

$$\begin{aligned} \dot{\psi} = & \frac{1 + \rho_2^2}{2\rho_2} [\mu\rho_2 \cos \beta + \nu\rho_1 \cos(\beta + \psi)] \\ & - \frac{1 + \rho_1^2}{2\rho_1} [\mu\rho_1 \cos \beta + \nu\rho_2 \cos(\beta - \psi)], \end{aligned} \quad (4)$$

on domain $D = \{(\rho_1, \rho_2, \psi) | 0 \leq \rho_{1,2} \leq 1, -\pi \leq \psi \leq \pi\}$.

Phase space is visualized using cylindrical coordinates (ρ_1, ψ, ρ_2) , see Figure 2. The translation $\Pi : \beta \mapsto \beta + \pi$ reverses time in Eqs. (2)-(4), thus inverting flow in phase space and stability of fixed points; we restrict our attention to $0 \leq \beta \leq \pi$ in what follows.

a. Invariant Manifolds and fixed points. Analysis of equations (2)-(4) reveals the existence of two invariant surfaces defined by $S_\sigma = \{(\rho_1, \rho_2, \psi) | \rho_\sigma = 1\} \subset D$ [the top (blue) and lateral (red) surfaces of the cylinder displayed in Figure 2]. The dynamics on these manifolds were studied previously [13]: chimera states are born in a saddle-node bifurcation and undergo a Hopf bifurcation for larger coupling disparity $A = \mu - \nu$. The resulting stable limit cycle grows with A until eventually it is destroyed in a homoclinic bifurcation. Here, we generalize the previous analysis by considering the entire three-dimensional phase space D .

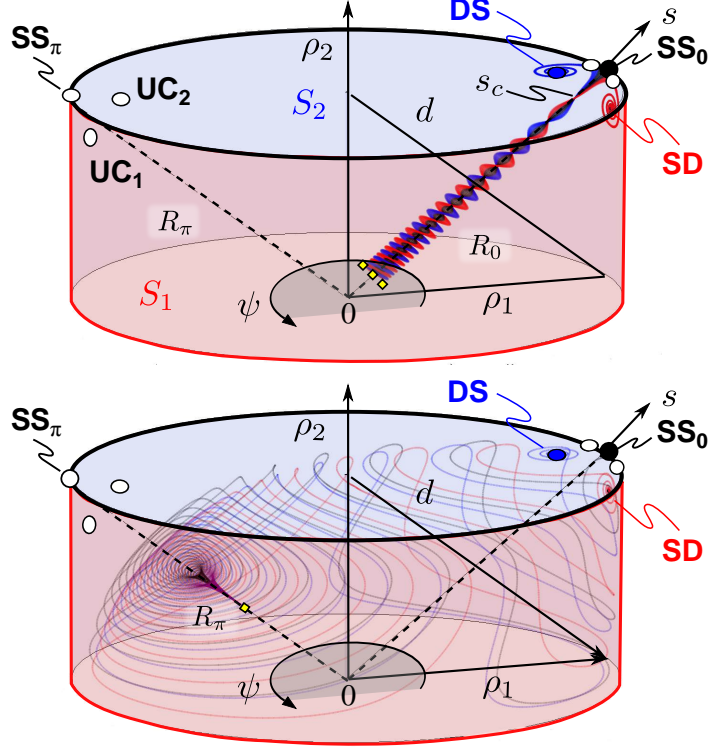


Figure 2. State variables (ρ_1, ψ, ρ_2) are interpreted as cylindrical coordinates. Phase space is structured by (i) two invariant rays, R_0 and R_π (dashed); and (ii) two invariant surfaces, S_1 and S_2 , forming the side and top surfaces of the cylinder slab. Except for a set of measure zero, all trajectories converge to one of three locations: SD chimera state on S_1 (red), DS (blue) chimera state on S_2 (blue), or fully synchronized state SS_0 (black). $(A, \beta) = (0.2, 0.025)$; filled/empty circles denote stable/unstable fixed points. Smaller yellow dots denote initial conditions.

Numerically, we observe that all trajectories with initial conditions $\rho_1, \rho_2 < 1$ are attracted to one of the invariant surfaces. From there, any of three attractors can be asymptotically approached: (i) a partially synchronized limit point (stable chimera, either SD or DS), (ii) a limit cycle (breathing chimera, either SD or DS), or (iii) the fully synchronized state SS_0 at $(\rho_1, \rho_2, \psi) = (1, 1, 0)$. Furthermore, unstable fixed points exist: a fully synchronized state SS_π at $(\rho_1, \rho_2, \psi) = (1, 1, \pi)$, and several unstable saddle chimeras (UC) [6, 15]. The dynamics on S_1 and S_2 are related due to the invariance of Eqs. (2)-(4) under the symmetry operation $\Sigma : (\rho_1, \rho_2, \psi) \mapsto (\rho_2, \rho_1, -\psi)$.

Outside of S_1 and S_2 , trajectories follow a complex winding motion, structured around the two invariant rays R_0 and R_π defined by $\rho_1 = \rho_2$ with $\psi = 0$ and $\psi = \pi$, respectively (see Figure 2 and [15]). Other than the origin, which is a repeller, there are no fixed points for $\rho_1, \rho_2 < 1$ [15], thus limit cycles in the interior of the phase space are also absent. In principle, a chaotic attractor could appear inside D but is not observed.

b. Destination Maps. First insights regarding basins of attraction for chimera states were gathered via simple Monte Carlo integration of uniformly distributed random initial conditions for $\rho_1, \rho_2 \in [0, 1]$ and $\psi \in [-\pi, \pi]$. These computations reveal that the probability $p(A, \beta)$ of ending up in a chimera state depends primarily on β with a maximum value for $\beta \rightarrow 0$ [15]. This approach provides information about the sizes of the basins of attraction, but it reveals little about their structure. We therefore ask: how is the three-dimensional phase space structured?

To better reflect symmetries of the phase space, the dynamics may be re-expressed in terms of the sum and difference of the order parameters (see Figure 2), $s = \frac{1}{2}(\rho_1 + \rho_2)$ with $0 \leq s \leq 1$, and $d = \frac{1}{2}(\rho_1 - \rho_2)$, with $-a(s) \leq d \leq a(s)$ where $a(s) = \frac{1}{2} - |\frac{1}{2} - s|$ [15].

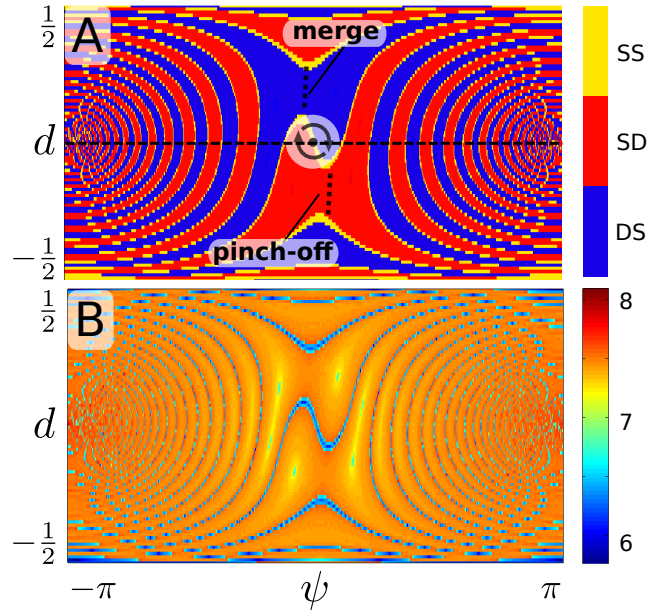


Figure 3. (A) Destination map section in the (d, ψ) -plane with $s = 0.56625 < s_c$, for SD (red), DS (blue) and SS₀ (yellow) states. When s increases, the boundaries of the basins of attraction perform a spiraling motion as indicated by arrows. (B) The logarithmic times $\log T$ to destination reflect the structure of the destination map in (A). Times peak at the interface boundaries between SS₀ and SD/DS regions (see also Figure 4). Parameters are $(A, \beta) = (0.1, 0.025)$.

In order to characterize the structure of the basins of attraction, we compute the destination maps for a set of initial conditions (s, d, ψ) . Figure 3A shows a typical cross-section of the destination map with fixed s : basins form a spiraling structure around R_π (the point $(d, \psi) = (0, \pi)$), with SD and DS basins always separated by the (often thin) basin for SS₀. The thickness of the basin spiral arms increases away from R_π , with maximum near R_0 (the point $(d, \psi) = (0, 0)$).

The area ratio between basins for SD (or, by symmetry, DS) and SS₀ is related to the probability that a

random initial condition will lead to a chimera state, and depends on parameters A and β as follows. For $\beta \rightarrow 0$, the SS_0 basin occupies an infinitesimal fraction of the area. As β increases, the SS_0 basin increases its area until it occupies the entire plane at $\beta = \beta_{SN}(A)$ when the chimera state is annihilated through a saddle-node bifurcation. For $A < A_{SN}(\beta)$ or $A > A_{HC}(\beta)$, no chimera state exists and the entire basin belongs to the SS_0 state. With increasing $A > A_{SN}$, the (total) basin area of SS_0 gradually decreases from 100% until it saturates near the homoclinic bifurcation [15].

As s increases from zero, basins merge and pinch-off in an alternating fashion [15] so that the basin boundaries rotate counter-clockwise about R_0 [$(d, \psi) = (0, 0)$ in Figure 3A]. Once s reaches $s_c \approx \sqrt{1 - A}$, this rotation stops, demonstrating that knowledge of the trajectory position in the $s = s_c$ plane is sufficient for determining its final fate.

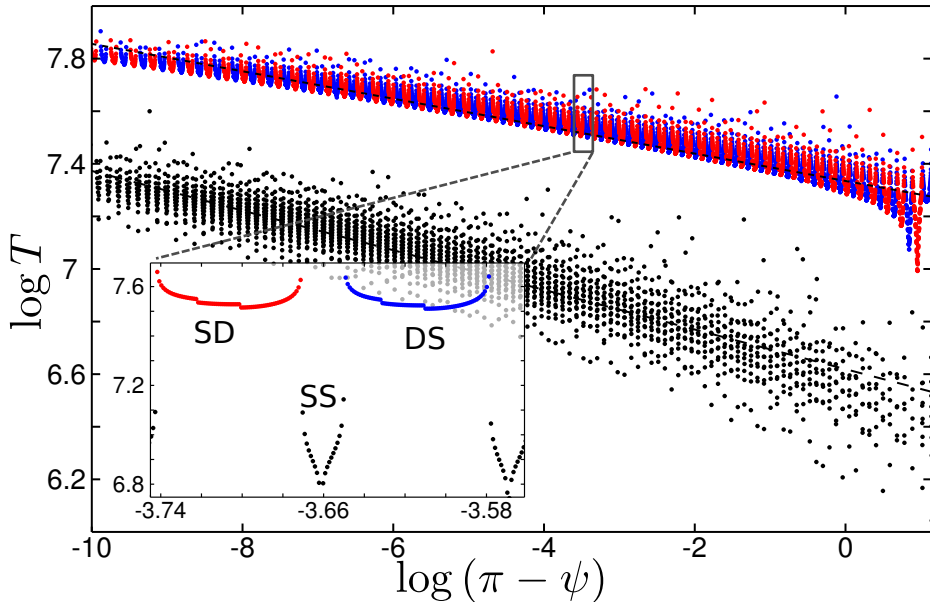


Figure 4. Times T to reach ϵ -neighborhood of fixed points $SS_0/DS/SD$; trajectories start from $(s, d, \psi) = (0.56625, 0, \psi)$ for $-\pi \leq \psi \leq \pi$, $A = 0.1, \beta = 0.025$ (straight line on Figure 3). Average destination times T grow like a power law as $\psi \rightarrow \pm\pi$, thus basin structure is self-similar around $(d, \psi) = (0, \pi)$. T diverges at the boundary between SD/DS and SS_0 basins (inset), since these trajectories lie on stable manifolds leading to saddle points on invariant manifolds S_1, S_2 .

The basin density appears singular near R_π , with a nested structure that allows even tiny perturbations of the initial condition to strongly influence the final state. More generally, the highly alternating basin structure is reflected in the times to reach steady-state attractors, which are displayed in Figure 3 B. Figure 4 shows destination times T along a section of that figure between the origin and $(d, \psi) = (0, \pi)$, revealing a power-law behavior that may result from this nested spiral arm basin structure.

Figure 4 also reveals that destination times diverge on the basin boundaries (see inset), which is explained by the fact that these boundaries form separatrix sheets: these are the two-dimensional stable manifolds emanating from the saddle chimeras on S_1 and S_2 , originating in the saddle-node bifurcation that gives birth to chimeras, see Figure 2 and [13]. Numerical continuation of those sheets [15] displays the same twisting motion as seen in Figure 3.

c. *Analysis.* A complete analysis of the basins for the entire phase space is difficult to achieve, but the main features of the basin structure have their origin in the invariant rays R_0 and R_π about which a perturbative analysis can be made. Near R_0 , we make the ansatz:

$$\begin{aligned}\psi &= \psi_1 \epsilon + \mathcal{O}(\epsilon^2), & d &= d_1 \epsilon + \mathcal{O}(\epsilon^2), \\ \beta &= \beta_1 \epsilon + \mathcal{O}(\epsilon^2), & A &= A_1 \epsilon + \mathcal{O}(\epsilon^2).\end{aligned}$$

(keeping in mind that $A > 2\beta$ is required for existence of a chimera state in this limit [13]). After a change of variables $d_1 = r \cos \theta = d_1$, $\frac{1}{2}s\psi_1 = r \sin \theta$, performing an averaging procedure [15] we find

$$\frac{dr}{dt} = -\beta_1 s^2 r \epsilon \quad (5)$$

$$\frac{d\theta}{dt} = \frac{1}{2} (1 - s^2 - A_1 \epsilon) \quad (6)$$

$$\frac{ds}{dt} = \frac{1}{2} s (1 - s^2) \beta_1 \epsilon. \quad (7)$$

The evolution of θ is an order of magnitude faster than that of r and s , suggesting that trajectories are spirals around the R_0 manifold. As $t \rightarrow \infty$, the radius r goes to 0, hence trajectories slowly converge toward R_0 until the approximations break down when $\frac{d\theta}{dt} = 0$ and higher order terms become significant. In other words, this manifold is weakly attracting. The frequency of rotation is $\omega = \frac{1}{2}(1 - s^2 - A_1 \epsilon)$. So, as we observed numerically, the rotation frequency $d\theta/dt \rightarrow 0$ as $s \rightarrow s_c \approx \sqrt{1 - A}$, at which point trajectories cease to have a spiral character and instead separate, evolving toward the fully synchronized state or the DS or SD chimeras.

By symmetry, if a trajectory originating at (s, d, ψ) converges to the SD state, the trajectory originating at $(s, -d, -\psi)$ must converge to the DS state. Therefore, the position relative to a separating boundary in the s_c plane determines the final state. Numerical integration confirms that trajectories converging to SD and DS chimeras form opposing sides of a positively oriented double helix centered on R_0 (red and blue in Figure 2 and [15]). The ‘‘rotation’’ of the basin boundary as s increases along the R_0 manifold (indicated symbolically in Figure 3 A) can also be understood analytically in the perturbative limit close to R_0 . The boundary angle is proportional to $\beta^{-1} \ln(1 - A/2) - \beta^{-1} \ln(s)$, yielding a rotation rate of $(\beta s)^{-1}$ as the section plane s varies uniformly [15].

Analysis around the R_π ray can be performed by a similar ansatz with $\psi = \pi + \psi_1\epsilon + \mathcal{O}(\epsilon^2)$. After an analogous change of variables [15], we obtain

$$\frac{dr}{dt} = \frac{1}{2}\beta_1 r\epsilon \quad (8)$$

$$\frac{d\theta}{dt} = -\frac{1}{2}\sqrt{1-s^4} \left[1 - A_1\epsilon/(s^2+1) \right] \quad (9)$$

$$\frac{ds}{dt} = \frac{1}{2}s(1-s^2)\beta_1 A_1\epsilon^2. \quad (10)$$

This reveals a spiraling motion around the R_π manifold in which the radius diverges exponentially. In contrast to the previous case, the derivative of θ is an order of magnitude larger than the derivative of r and two orders of magnitude larger than the derivative of s . This means that the rotation around the R_π manifold and the divergence away from the manifold occur more quickly than the translation along the manifold. In other words, each trajectory (and consequently any basin boundary) winds around R_π within a plane with (approximately) fixed s (see cross section in Figure 3 and [15]).

d. Discussion. The probability that a random initial condition ends up in a chimera state, while relevant for real-world applications, has not been a frequent topic of investigation [1, 6]. Here, we have provided a detailed mathematical analysis unveiling the basin structure for a very simple system with two populations, allowing for insight into the chimera's relative rarity.

The stable manifolds of the saddles on $S_{0,\pi}$ divide phase space into singly connected basins of attraction [15]. Basins near the fully synchronized (SS_0) and chimera (SD/DS) states are simple in structure and relatively large², resulting in robustness to perturbations. The twisting motion around the invariant rays $R_{0,\pi}$, however, yields a complex basin structure which we explain analytically. As one approaches R_π , the basin density diverges, and basins are *locally* intermingled [16]: perturbations in this region affect the fate of a trajectory drastically.

Sampling the immense initial state space associated with the case of $N < \infty$ would be a burdensome task. Our analysis was facilitated by considering $N \rightarrow \infty$, allowing us to focus on the low-dimensional order parameter dynamics on the OA-manifold [14]. While the higher dimensional and richer dynamics away from this manifold poses a challenge in its own right [6], the continuum theory allows us to gain useful insight by mapping the discrete to the continuous order parameter, $R^\sigma e^{i\Phi^\sigma} \approx \rho^\sigma e^{i\phi^\sigma}$ (identity for $N \rightarrow \infty$). While bifurcation boundaries may blur for very low N and the finely filigreed basin boundaries near R_π may break down, general basin structures will look similar even for moderate N . In particular, continuum theory gives us powerful means to construct initial phase densities, via $f^\sigma(\theta, t) = \frac{1}{2\pi} \left[1 + \sum_{n=1}^{\infty} \rho_\sigma^n e^{in(\theta-\phi_\sigma)} + c.c. \right]$ [15], leading to chimera states. Given initial phases θ_k sampled uniformly on $[-\pi, \pi]^n$, the probability distribution for R_σ is unimodal with mean $\mu \sim N^{-1/2}$ and

² Local basin volumes of chimeras presumably scale like $|\mathbf{x}_{\text{SD,DS}} - \mathbf{x}_{\text{SADDLE}}|$

variance $\sigma \sim N^{-1}$. The probability distribution for Φ_σ is invariant and uniform; this observation combined with the intermingled basin structure near R_π explains why in practice random initial phases can lead to both chimera and fully synchronized states.

While two populations allow for the multi-stability between the fully synchronous state (SS_0) and two symmetrically equivalent chimera states (SD and DS), generalizations of such hierarchical structure to $n > 2$ populations [13, 17] make accessible larger configuration spaces of size 2^n by variation and permutation of the synchronization-desynchronization patterns. Biologically, systems with multiple coexisting chimera attractors have been proposed to describe ‘metastable dynamics’ required to modulate neural activity patterns [18], or to encode memory. Indeed, localized dynamical states are directly related to function in neural networks [19]; localized synchrony is generally regarded to play a role in memory formation and spatially localized activity has been widely studied in neural field models as bump states [20], which can be modeled using theta-neurons [21] and are phenomenologically similar to chimera states. It is worth noting that chimeras occur in models of neural activity [6, 22–24].

Technological implementations of chimera states could be achieved in micro-(opto)-electro-mechanical oscillators [25] where synchronization patterns could modulate a technical function. Conversely, as power grid network topologies evolve to incorporate growing sources of renewable power, the resulting decentralized, hierarchical networks [26] may be threatened by chimera states, which could lead to large scale partial blackouts and unexpected behavior.

The potential for applications—or threats—makes the dynamic re-configuration and switching between chimera configurations (possibly modulating functional properties of the underlying oscillator network) particularly relevant [27]; applications that modulate these functional properties can only be achieved using detailed knowledge of the basin structure. With our results, it should be possible to construct efficient control strategies to stabilize or prevent chimera states, with applications across many fields.

One may wonder if any of the structures studied here retains relevance in cases of more than two populations. It can be shown that the invariant hyper-ray corresponding to R_0 defined by $\rho_\sigma = \rho$ and $\phi^\sigma = 0$ exists for $n > 2$, and that the flow on this ray is $\rho \rightarrow 1$. This suggests that the phase space is skeletonized similarly and a similar analysis may be feasible—a task left for a future study.

While we have revealed the basin boundary structure for chimera states by analyzing the full state space of the order parameters using recent reduction methods [14], it remains an exciting challenge to show whether similar efforts bear fruit by attempting an analysis of other models where reduction methods have become available only very recently [21, 28], and to examine how our results translate to these cases.

ACKNOWLEDGMENTS

Research supported by the Dynamical Systems Interdisciplinary Network, University of Copenhagen (EAM). We thank C. Bick, R. Mirolo, S. Strogatz and O. Omel'chenko for helpful conversations and comments.

- [1] C. Huygens, *Oeuvres Complètes* (Swets & Zeitlinger Publishers, Amsterdam, 1967) p. Vol. 15; S. H. Strogatz, D. M. Abrams, A. McRobie, B. Eckhardt, and E. Ott, *Nature* **438**, 43 (2005); K. Wiesenfeld, P. Colet, and S. Strogatz, *Phys. Rev. E* **57**, 1563 (1998); M. B. Elowitz and S. Leibler, *Nature* **403**, 335 (2000); J. Buck and E. Buck, *Science* **159**, 1319 (1968); C. S. Peskin, *Mathematical aspects of heart physiology* (Courant Inst. of Math. Sciences Publication, New York, 1975) pp. 268–275; D. Michaels, E. Matyas, and J. Jalife, *Circ. Res.* **61**, 704 (1987); C. Liu, D. R. Weaver, S. H. Strogatz, and S. M. Reppert, *Cell* **91**, 855 (1997); I. Z. Kiss, Y. Zhai, and J. L. Hudson, *Science (New York, N.Y.)* **296**, 1676 (2002); A. F. Taylor, M. R. Tinsley, F. Wang, Z. Huang, and K. Showalter, *Science (New York, N.Y.)* **323**, 614 (2009); T. M. Massie, B. Blasius, G. Weithoff, U. Gaedke, and G. F. Fussmann, *Proc. Nat. Acad. Sci.* **107**, 4236 (2010); A. Ghosh, B. Chance, and E. Pye, *Arch. Biochem. and Biophys.* **145**, 319 (1971); S. Dano, P. G. Sorensen, and F. Hynne, *Nature* **402**, 320 (1999).
- [2] Y. Kuramoto and D. Battogtokh, *Nonlin. Phenom. in Comp. Sys.* **4**, 380 (2002); E. A. Martens, S. Thutupalli, A. Fourrière, and O. Hallatschek, *Proc. Natl. Acad. Sci.* **110**, 10563 (2013).
- [3] M. Wickramasinghe and I. Z. Kiss, *PLoS One* **8**, e80586 (2013).
- [4] M. R. Tinsley, S. Nkomo, and K. Showalter, *Nature Physics* **8**, 1 (2012).
- [5] A. M. Hagerstrom, T. E. Murphy, R. Roy, P. Hövel, I. Omelchenko, and E. Schöll, *Nature Physics* **8**, 1 (2012).
- [6] S. I. Shima and Y. Kuramoto, *Phys. Rev. E* **69**, 036213 (2004); D. Abrams and S. Strogatz, *Phys. Rev. Lett.* **93**, 1 (2004); O. E. Omel'chenko, Y. L. Maistrenko, and P. A. Tass, *Phys. Rev. Lett.* **100**, 044105 (2008); A. Pikovsky and M. Rosenblum, *ibid.* **264103**, 1 (2008); C. R. Laing, *Chaos (Woodbury, N.Y.)* **19**, 013113 (2009); C. R. Laing, K. Rajendran, and I. G. Kevrekidis, *Chaos* **22**, 013132 (2012); S. Olmi, A. Politi, and A. Torcini, *EPL (Europhysics Letters)* **92**, 60007 (2010); M. J. Panaggio and D. M. Abrams, *ibid.* **110**, 094102 (2013); *Phys. Rev. E* **91**, 022909 (2015); *Nonlinearity* **28**, R67 (2015); Y.-E. Feng and H.-H. Li, *Chinese Physics Letters* **32**, 060502 (2015).
- [7] C. R. Laing, [arXiv:1506.05871 \[nlin-PS\]](https://arxiv.org/abs/1506.05871).
- [8] G. C. Sethia and A. Sen, *Phys. Rev. Lett.* **112**, 144101 (2014); L. Schmidt, K. Schönleber, K. Krischer, and V. García-Morales, *Chaos* **24**, 013102 (2014).
- [9] J. Phillips, H. V. der Zant, J. White, and T. Orlando, *Phys. Rev. B* **47** (1993).
- [10] N. V. Swindale, *Proc. Roy. Soc. London. B.* **208**, 243 (1980); J. D. Murray, *Mathematical Biology I: An Introduction*. 2002 (2002).
- [11] A. E. Motter, *Nature Physics* **6**, 164 (2010).

- [12] P. J. Menck, J. Heitzig, N. Marwan, and J. Kurths, *Nature Physics* **9**, 1 (2013).
- [13] D. M. Abrams, R. E. Mirollo, S. H. Strogatz, and D. A. Wiley, *Phys. Rev. Lett* **101**, 084103 (2008); E. Montbrió, J. Kurths, and B. Blasius, *Phys. Rev. E* **70**, 056125 (2004); C. R. Laing, *Chaos* **22**, 043104 (2012); E. A. Martens, *Chaos (Woodbury, N.Y.)* **20**, 043122 (2010); *Phys. Rev. E* **82**, 016216 (2010).
- [14] E. Ott and T. M. Antonsen, *Chaos (Woodbury, N.Y.)* **18**, 037113 (2008); *Chaos* **023117** (2009); E. Ott, B. R. Hunt, and T. M. Antonsen, *Chaos (Woodbury, N.Y.)* **21**, 025112 (2011).
- [15] “ See Supplemental Material in the Ancillary Files on *arXiv* or at http://eam.webhop.net/papers/chimeraBOA_arXiv_SUPP_v12.pdf for a derivation of equations (2) to (4), a derivation of the invariant manifolds and fixed points, results and details on basin size estimations using Monte Carlo integration, governing equations in s and d coordinates, the method used to compute destination maps, a movie of the pinching and merging of basin boundaries for increasing s , numerical continuation and visualization of separatrix sheets, and perturbative calculations near R_0 and R_π manifolds.”.
- [16] E. Ott, J. Alexander, I. Kan, J. Sommerer, and J. Yorke, *Physica D: Nonlinear Phenomena* **76**, 384 (1994).
- [17] M. Shanahan, *Chaos (Woodbury, N.Y.)* **20**, 013108 (2010).
- [18] X. Wang, *Physiological reviews* , 1195 (2010).
- [19] J. Fell and N. Axmacher, *Nat. Rev. Neurosci.* **12**, 105 (2011); D. H. Hubel, *Journal of Physiology* **147**, 226 (1958).
- [20] S. Amari, *Biological Cybernetics* **27**, 77 (1977); C. R. Laing and C. C. Chow, *Neural computation* **13**, 1473 (2001).
- [21] C. Laing, *Phys. Rev. E* , 1 (2014).
- [22] H. Sakaguchi, *Phys. Rev. E* **73**, 1 (2006).
- [23] J. Cabral, E. Hugues, O. Sporns, and G. Deco, *NeuroImage* **57**, 130 (2011).
- [24] J. Hizanidis, V. G. Kanas, A. Bezerianos, and T. Bountis, *Int. Jour. Bif. and Chaos* **24**, 1450030 (2014).
- [25] M. Eichenfield, J. Chan, R. M. Camacho, K. J. Vahala, and O. Painter, *Nature* **462**, 78 (2009); G. Heinrich, M. Ludwig, J. Qian, B. Kubala, and F. Marquardt, *Phys. Rev. Lett.* **107**, 8 (2011).
- [26] M. Rohden, A. Sorge, M. Timme, and D. Witthaut, *Phys. Rev. Lett.* **109**, 064101 (2012); A. Motter and S. Myers, *Nature ...* **9**, 1 (2013).
- [27] C. Bick and E. A. Martens, *New Journal of Physics* **17**, 033030 (2015).
- [28] D. Pazó and E. Montbrió, *Phys. Rev. X* **4**, 1 (2014).

Basins of Attraction for Chimera States

Supplemental Material

Erik A. Martens^{a,b,*}, Mark J. Panaggio^{c,d}, and Daniel M. Abrams^{d,e,f}

^a*Dept. of Biomedical Sciences, University of Copenhagen, Blegdamsvej 3, 2200 Copenhagen, Denmark*

^b*Dept. of Mathematical Sciences, University of Copenhagen, Universitetsparken 5, 2200 Copenhagen, Denmark*

^c*Mathematics Dept., Rose-Hulman Institute of Technology, Terre Haute, Indiana 47803*

^d*Dept. of Engineering Sciences and Applied Mathematics, Northwestern University, Evanston, Illinois 60208*

^e*Dept. of Physics and Astronomy, Northwestern University, Evanston, Illinois 60208*

^f*Northwestern Institute on Complex Systems, Northwestern University, Evanston, Illinois 60208, USA*

Keywords: chimera states, basins of attraction, hierarchical network structure, control, neural networks

I. REDUCTION TO OTT-ANTONSEN MANIFOLD IN THE THERMODYNAMIC LIMIT $N \rightarrow \infty$

We consider the Kuramoto-Sakaguchi model with non-local coupling between n populations [1]

$$\dot{\theta}_k^\sigma = \omega + \sum_{\sigma'=1}^n \frac{K_{\sigma\sigma'}}{N^{\sigma'}} \sum_{l=1}^{N^{\sigma'}} \sin(\theta_l^{\sigma'} - \theta_k^\sigma - \alpha), \quad (1)$$

where θ_k^σ is the phase of the k th oscillator $k = 1, \dots, N^\sigma$ belonging to population $\sigma = 1, \dots, n$. To facilitate comparison with previous work [1], we consider the case of symmetric coupling with $K_{\sigma\sigma'} = K_{\sigma'\sigma}$. The phase lag parameter α tunes between the regimes of pure sine-coupling ($\alpha = 0$) and pure cosine-coupling ($\alpha = \pi/2$). In what follows, we introduce the re-parameterized phase lag parameter $\beta = \pi/2 - \alpha$, since for this type of system chimeras emerge in the limit of cosine-coupling [1], i.e. $\beta \rightarrow 0$.

To make further progress, we consider the thermodynamic limit, i.e., the case of $N^\sigma \rightarrow \infty$ oscillators per population. This allows for a description of the dynamics in terms of the mean-field order parameter [2]. Eqs. (1) then give rise to the continuity equation

$$\frac{\partial f^\sigma}{\partial t} + \frac{\partial}{\partial \theta}(f^\sigma v^\sigma) = 0, \quad (2)$$

where $f^\sigma(\theta, t)$ is the probability density of oscillators in population σ , and $v^\sigma(\theta, t)$ is their velocity, given by

$$v^\sigma(\theta, t) = \omega + \sum_{\sigma'=1}^n K_{\sigma\sigma'} \int e^{i\theta'} f^{\sigma'}(\theta', t) d\theta'. \quad (3)$$

Here we have dropped the superscripts to simplify notation: θ means θ^σ , and θ' means $\theta^{\sigma'}$. Following Ott and Antonsen [2], we consider probability densities along a manifold given by

$$f^\sigma(\theta, t) = \frac{1}{2\pi} + \frac{1}{2\pi} \sum_{n=1}^{\infty} [a_\sigma^*(t) e^{i\theta}]^n + c.c. \quad (4)$$

where $*$ denotes complex conjugation and $a_\sigma(t)$ is given by

$$a_\sigma(t) = \int e^{i\theta} f^\sigma(\theta, t) d\theta. \quad (5)$$

Defining $a_\sigma(t) = \rho_\sigma(t) e^{i\phi_\sigma(t)}$ where ρ_σ and ϕ_σ represent mean-field order parameters, the governing equation can be reduced to the system [1, 3]

$$\dot{\rho}_\sigma = \frac{1 - \rho_\sigma^2}{2} \sum_{\sigma'=1}^n K_{\sigma\sigma'} \rho'_\sigma \sin(\phi_{\sigma'} - \phi_\sigma + \beta) \quad (6)$$

$$\dot{\phi}_\sigma = \omega - \frac{1 + \rho_\sigma^2}{2\rho_\sigma} \sum_{\sigma'=1}^n K_{\sigma\sigma'} \rho'_\sigma \cos(\phi_{\sigma'} - \phi_\sigma + \beta). \quad (7)$$

* erik.martens@ds.mpg.de

The Ott/Antonsen manifold, in which the Fourier coefficients $f_n(t)$ of the probability density f satisfy $f_n(t) = a(t)^n$, is globally attracting for a frequency distribution with non-zero width Δ [2]. For identical oscillators ($\Delta = 0$), the dynamics for the problem (with $n = 2$ populations) can be described by reduced equations using the Watanabe/Strogatz ansatz [4], as shown in Pikovsky and Rosenblum [5]; the authors showed that Eqs. (1) may also be subject to more complicated dynamics than those described by the Ott/Antonsen ansatz. Studies by Laing [6, 7] investigated the dynamics using the Ott/Antonsen ansatz for $n = 2$ populations for the case of non-identical frequencies and found that the dynamics for sufficiently small Δ is qualitatively equivalent to the dynamics obtained for $\Delta = 0$. It is therefore justified to discuss the dynamics for $N \rightarrow 0$ representing the case of *nearly* identical oscillators $\Delta \rightarrow 0$ using the Ott/Antonsen reduction.

II. GOVERNING EQUATIONS FOR TWO POPULATIONS

We restrict our attention to the case of $n = 2$ populations. Accordingly, we define the coupling parameters $K_{11} = K_{22} = \mu$ and $K_{12} = K_{21} = \nu$; by rescaling time we can eliminate one parameter so that $1 = \mu + \nu$ without loss of generality. The remaining parameter is redefined via $A = \mu - \nu$, expressing the disparity of coupling between the two neighboring populations. By virtue of the translational symmetry, $\phi_\sigma \rightarrow \phi_\sigma + \text{const.}$, the dynamics of the system is effectively three dimensional. We introduce the angular phase difference $\psi = \phi_1 - \phi_2$ of the order parameter, and the resulting governing equations become

$$\dot{\rho}_1 = \frac{1 - \rho_1^2}{2} [\mu \rho_1 \sin \beta + \nu \rho_2 \sin (\beta - \psi)], \quad (8)$$

$$\dot{\rho}_2 = \frac{1 - \rho_2^2}{2} [\mu \rho_2 \sin \beta + \nu \rho_1 \sin (\beta + \psi)], \quad (9)$$

$$\begin{aligned} \dot{\psi} = & \frac{1 + \rho_2^2}{2\rho_2} [\mu \rho_2 \cos \beta + \nu \rho_1 \cos (\beta + \psi)] \\ & - \frac{1 + \rho_1^2}{2\rho_1} [\mu \rho_1 \cos \beta + \nu \rho_2 \cos (\beta - \psi)]. \end{aligned} \quad (10)$$

where the state variables lie in the domain $D = \{(\rho_1, \rho_2, \psi) \in \mathbb{R}^3 | 0 < \rho_1, \rho_2 \leq 1, \psi \in [-\pi, \pi]\}$.

To investigate the basins of attraction, it proves useful to express the dynamics in terms of the sums and difference of the order parameters, i.e., we define

$$s = \frac{1}{2}(\rho_1 + \rho_2), \quad (11)$$

$$d = \frac{1}{2}(\rho_1 - \rho_2), \quad (12)$$

and ψ as above. These variables belong to the domain defined by $\psi \in [-\pi, \pi]$, $s \in [0, 1]$ and $d \in [-a, a]$ with $a(s) = \frac{1}{2} - |\frac{1}{2} - s|$ (the back-transformation is $\rho_1 = s + d$ and $\rho_2 = s - d$, without the factor of 2.). The governing equations are then expressed as

$$\begin{aligned} \dot{s} = & \frac{1}{2} \{ s[\mu(1 - 3d^2 - s^2) + \nu(1 + d^2 - s^2) \cos \psi] \sin \beta \\ & + \nu d(1 - d^2 + s^2) \cos \beta \sin \psi \}, \end{aligned} \quad (13)$$

$$\begin{aligned} \dot{d} = & \frac{1}{2} \{ d[\mu(1 - d^2 - 3s^2) - \nu(1 - d^2 + s^2) \cos \psi] \sin \beta \\ & - \nu s(1 + d^2 - s^2) \cos \beta \sin \psi \}, \end{aligned} \quad (14)$$

$$\begin{aligned} \dot{\psi} = & (d^2 - s^2)^{-1} \{ -2ds \cos \beta [\mu(d^2 - s^2) + \nu \cos \psi] \\ & + [s^2 + d^4 + s^4 + d^2(1 - 2s^2)] \nu \sin \beta \sin \psi \}. \end{aligned} \quad (15)$$

Eqs. (8)-(10) or Eqs. (13)-(15), respectively, are invariant under the transformation $\Sigma : (\rho_1, \rho_2, \psi) \mapsto (\rho_2, \rho_1, -\psi)$, corresponding to interchanging the two oscillator populations. More generally, the change of parameters $\Pi : \beta \mapsto \beta + \pi$ reverses time in the governing equations, thus inverting flow and stability properties in phase space. This is also valid for the more general case of $n > 2$ equations, i.e., for Eqs. (6) and (7).

III. INVARIANT MANIFOLDS (IMS).

a. *Two-dimensional invariant manifolds.* Letting $\rho_1 \rightarrow 1$ in Eqs. (8)-(10) leaves ρ_1 invariant, i.e. $\dot{\rho}_1 = 0$. The same holds true for ρ_2 by symmetry. Thus we find two two-dimensional invariant surfaces, corresponding to the top and side surface of D ,

defined by

$$S_\sigma = \{(\rho_1, \rho_2, \Psi) \in S \mid \rho_\sigma = 1\}, \quad (16)$$

where $\sigma = 1, 2$ refers to the SD, DS manifolds, respectively. The dynamics in one manifold is identical to the other via the symmetry operation defined by operator Σ , see main text. The dynamics on these IMs is analyzed in [1].

b. One-dimensional invariant manifolds. Our numerical investigations indicate the presence of an invariant manifold at $\psi = 0, \pi$ with $\rho_1 = \rho_2$. Substituting these values into Eqs. (8)-(10), we get

$$\dot{s} = \frac{1}{2} \sin \beta \, s(1 - s^2), \quad (17)$$

$$\dot{d} = \dot{\psi} = 0. \quad (18)$$

The first equation implies that any initial point on the rays with $d = 0$ and $\psi = 0, \pi$ remains there for all times; if $0 < \beta < \pi$, the trajectory moves towards the SS_0 attractor according to (17). Thus, two invariant rays exist, defined via

$$R_\phi = \{(\rho_1, \rho_2, \Psi) \in D \mid \rho_1 = \rho_2 \text{ and } \psi = \phi\} \quad (19)$$

with $\phi = 0, \pi$.

Note that another one-dimensional invariant manifold S_{12} is defined as the intersection $S_1 \cap S_2$, and any initial point with $s = 1$ on S_{12} will therefore always end up in the SS_0 state.

A. Fixed points.

c. Fixed points on $S_{1,2}$. The fixed points in the $S_{1,2}$ manifolds are the SD, DS chimera states and fully synchronized SS_0 states that are discussed in detail in [1]; note that since S_{12} is an invariant manifold, there must be another fixed point in addition to SS_0 contained in it, with opposite stability: this source is found at $(\rho_1, \rho_2, \psi) = (1, 1, \pi)$, which we refer to as SS_π . Figure 2 (main text) illustrates how trajectories nearby are repelled from the ray R_π . On $S_{1,2}$, stable chimera states are born through a saddle node bifurcation, and undergo a Hopf bifurcation for sufficiently large disparity values A so that $\rho_\sigma < 1$ is oscillatory; the associated limit cycle is destroyed in a homoclinic bifurcation with even larger A .

d. Chimera states. In addition to the in-phase ($\rho_1 = \rho_2 = 1$ and $\psi = 0$) and anti-phase ($\rho_1 = \rho_2 = 1$ and $\psi = \pi$) equilibrium points, there are also three equilibrium points with $\rho_2 = 1$ and $\rho_1 \neq 1$ (and three analogous fixed points with $\rho_1 = 1$ and $\rho_2 \neq 1$) [3]. These equilibrium points represent chimera states. Numerics suggest that two of these equilibrium points occur near $\psi = 0$ and one occurs near $\psi = \pi$. Using an ansatz motivated by these numerical results, we find that these equilibrium points satisfy the following scaling relationships (where $A = \mu - \nu$ and $\mu + \nu = 1$):

i) Stable Chimera near $\psi = 0$ (DS):

$$\begin{aligned} \beta &\sim A\beta_1, \\ \rho_1 &\sim 1 - A \left(1 + \sqrt{1 - 4\beta_1^2} \right) + A^2 \left(1 - 4\beta_1^2 + \frac{1 - 6\beta_1^2}{\sqrt{1 - 4\beta_1^2}} \right), \\ \psi &\sim A(2\beta_1) + A^2 \left(\beta_1 \left[1 - \sqrt{1 - 4\beta_1^2} \right] \right). \end{aligned}$$

ii) Unstable Saddle Chimera near $\psi = 0$ (UC):

$$\begin{aligned} \beta &\sim A\beta_1, \\ \rho_1 &\sim 1 - A \left(1 - \sqrt{1 - 4\beta_1^2} \right) + A^2 \left(1 - 4\beta_1^2 - \frac{1 - 6\beta_1^2}{\sqrt{1 - 4\beta_1^2}} \right), \\ \psi &\sim A(2\beta_1) + A^2 \left(\beta_1 \left(1 + \sqrt{1 - 4\beta_1^2} \right) \right). \end{aligned}$$

iii) Unstable Chimera near $\psi = \pi$ (UC):

$$\begin{aligned} \beta &\sim A^{\frac{1}{2}}\beta_1, \\ \rho_1 &\sim 1 - A^2(2\beta_1^2) + A^3 \left(\frac{2}{3}\beta_1^4 \right), \\ \psi &\sim \pi - A^{\frac{3}{2}}(2\beta_1) + A^{\frac{5}{2}} \left(\frac{4}{3}\beta_1^3 - 2\beta_1 \right). \end{aligned}$$

These relationships are useful when trying to solve for the precise fixed point locations numerically and for approximating their stable and unstable manifolds in order to deduce the basin boundaries.

e. *Origin.* The origin is an unstable fixed point, as can be seen by linearizing for small ρ_1 and ρ_2 in Eqs. (8)–(10).

f. *Other fixed points.* Here we ask whether there are any fixed points off the invariant manifolds $S_{1,2}$: i.e., are there any fixed points with $\rho_1, \rho_2 \notin S_{1,2}$ where no population is completely synchronized? Together with Eqs. (8)–(10), $0 < \rho_1, \rho_2 < 1$ implies the following conditions:

$$0 = \mu\rho_1 \sin \beta + \nu\rho_2 \sin(\beta - \psi), \quad (20)$$

$$0 = \mu\rho_2 \sin \beta + \nu\rho_1 \sin(\beta + \psi), \quad (21)$$

$$\begin{aligned} 0 = \rho_1(1 + \rho_2^2) [\mu\rho_2 \cos \beta + \nu\rho_1 \cos(\beta + \psi)] \\ - \rho_2(1 + \rho_1^2) [\mu\rho_1 \cos \beta + \nu\rho_2 \cos(\beta - \psi)]. \end{aligned} \quad (22)$$

We know that $\beta \rightarrow \beta + \pi$ reverses time, so we can w.l.o.g. restrict our attention to $0 \leq \beta \leq \pi$. When $\beta = 0, \pi$, the first two equations are satisfied if $\psi = 0, \pi$. The third equation yields the solutions $\rho_2 = \pm\rho_1$ and $\rho_2 = \frac{\rho_1(1+A) \pm \sqrt{-4(-1+A)^2 + (3-A)(3A-1)\rho_1^2}}{2(A-1)}$, where only the first branch lies in $0 \leq \rho_{1,2} \leq 1$.

For all other cases, let us consider the equations by introducing $K = \mu/\nu > 1$ and $\rho_{\text{rel}} = \rho_2/\rho_1$:

$$0 = [\cos(\psi)\rho_{\text{rel}} + K] \sin \beta - \rho_{\text{rel}} \cos \beta \sin \psi, \quad (23)$$

$$0 = [K\rho_{\text{rel}} + \cos \psi] \sin \beta + \cos \beta \sin \psi, \quad (24)$$

$$\begin{aligned} 0 = -[2\rho_{\text{rel}}^2\rho_1^3 + (\rho_{\text{rel}}^2 - 1)\rho_1] \sin \psi \sin \beta \\ + [(1 - \rho_{\text{rel}}^2)\rho_1 \cos \psi + (\rho_{\text{rel}}^2 - 1)K\rho_{\text{rel}}\rho_1^3] \cos \beta. \end{aligned} \quad (25)$$

We note now that $\rho_{\text{rel}} > 0$ and $\sin \beta > 0$ by assumption and we can eliminate these expressions as follows

$$\frac{\cos \beta \sin \psi}{\sin \beta} = \frac{\cos(\psi)\rho_{\text{rel}} + K}{\rho_{\text{rel}}}, \quad (26)$$

$$\frac{\cos \beta \sin \psi}{\sin \beta} = -K\rho_{\text{rel}} - \cos \psi. \quad (27)$$

Equating (26) and (27), it follows that a fixed point with $0 < \rho_1, \rho_2 < 1$ and $0 < \beta < \pi$ can only exist if

$$0 = K\rho_{\text{rel}}^2 + 2\cos(\psi)\rho_{\text{rel}} + K, \quad (28)$$

which has the solutions

$$\rho_{\text{rel}} = -\frac{\cos \psi \pm \sqrt{\cos^2(\psi) - K^2}}{K}. \quad (29)$$

However, by assumption, we have $K > 1$ and the solutions are complex. Therefore, even if we find real values ψ, ρ_1 that satisfy the third fixed point equation (25), there will be no real solutions for ρ_{rel} , and thus also not for ρ_2 . Therefore fixed points in the interior of the domain can be excluded when $\beta \neq n\pi$ where n is an integer.

IV. NUMERICAL ANALYSIS

A. Probabilistic measure of basins of attraction

In order to obtain an estimate of the sizes of the basins of attraction of the equilibria of (8)–(10), we selected 1000 random initial points (ρ_1, ρ_2, ψ) . Eqs. (8)–(10) were then integrated for a sweep of parameter values of $0.01 \leq A \leq 0.49$ with increments of 0.01 and $0.005 \leq \beta \leq 0.245$ with increments of 0.005 until a final state was detected. The contour plot in supplemental Fig. S1 displays the fraction of those trajectories with final states near a chimera state.

It should be noted that the numerical experiment above assumes that ρ_1, ρ_2 , and ψ are uniformly distributed. For systems with a finite number of oscillators N^σ in each population, the expected value of the order parameter value ρ_σ is $\mathcal{O}(N^{-1/2})$. Hence, the probabilities computed using the above scheme should not be interpreted as the probability that a state with randomly selected initial phases $\theta_k^{(\sigma)}$ would evolve toward a chimera state. Instead, they represent the size of the basins of attraction of the chimera states relative to the size of the basin of attraction of the fully synchronized state in the continuum limit $N^\sigma \rightarrow \infty$.

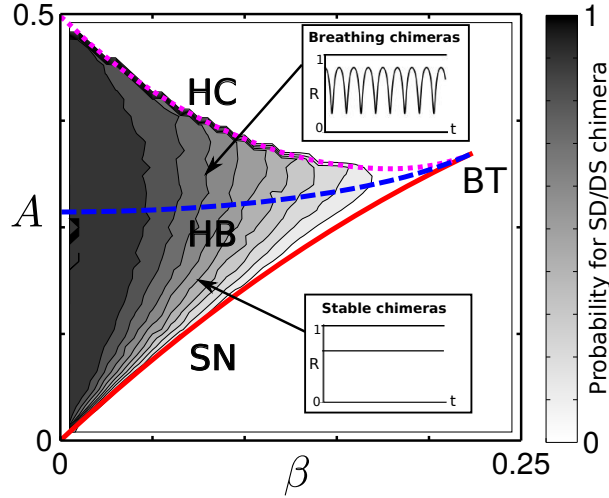


FIG. S1. Probabilities to obtain chimera states via random sampling of initial conditions (ρ_1, ρ_2, ψ) . Chimeras appear within the wedge defined by a saddle-node bifurcation (SN, solid) for small A and a homoclinic bifurcation (HC, dotted) for large A [1]. For intermediate A , the asynchronous order parameter undergoes a Hopf bifurcation (HB, dashed). Probabilities for ending up in either SD/DS chimera were measured by realizing 1000 random initial conditions (ρ_1, ρ_2, ψ) for each parameter value set.

B. Destination Maps

Simulations for a given initial condition were carried out until trajectories to a fully synchronized (limit point, LP) or a stable (LP) or breathing chimera (limit cycle LC) occurred. The detection of these three types of states was carried out in two steps, described below. Integration of Eqs. (8)-(10) or (13)-(15) were carried out in Matlab™ using the `ode45` solver routine with event detection on a high performance computation cluster, with a relative error tolerance of 10^{-8} . Algorithms below are outlined for (ρ_1, ρ_2, ψ) -coordinates; analogous detections for (s, d, ψ) -coordinates are carried out by applying the related coordinate transformations. Below, $d\rho_{1,2} \approx \dot{\rho}_{1,2} dt$ and $d\psi \approx \dot{\psi} dt$ denote the approximate differential values evaluated by the o.d.e. integrator at discrete time steps.

C. Simple convergence test (Event A)

This simple test was used to detect the type of state asymptotically achieved. Integration was stopped by an event detection algorithm solving for roots of:

- LP detection: $v = [d\rho_1^2 + d\rho_2^2 + d\psi^2]^{1/2} - \delta$: convergence to any LP (in any direction).
- Convergence to LC on S_1 : $v = [(\rho_1 - 1)^2 + d\rho_2^2] - \delta$ [passage through $\dot{\rho}_2 = 0$ (= 1 cycle), positive direction].
- Convergence to LC on S_2 : $v = [(\rho_2 - 1)^2 + d\rho_1^2] - \delta$ [passage through $\dot{\rho}_1 = 0$ (= 1 cycle), positive direction].

A convergence tolerance of $\delta \sim 10^{-6}$ was chosen.

D. Estimating time to attractor

The following algorithm is adopted for obtaining estimates for the time to reach the attractor, T , i.e., the traveling time from initial to end condition. When these times are not of interest, the previous scheme is preferred due to significant gains in computational speed.

1. Integration is carried out until $v = [d\rho_1^2 + d\rho_2^2 + d\psi^2]^{1/2} - \delta$ crosses a zero (**Event B**, LP detection).
2. If the integration fails to detect a fixed point, the algorithm enters a loop of max. 100 iterations, where:
 - i.) Integration is carried out to detect $k = 1, \dots, 10$ events of type **Event A**, limit point and limit cycles). Periods of limit cycles and event states $(\rho_1, \rho_2, \psi)|_{t=t_k}$ are stored.

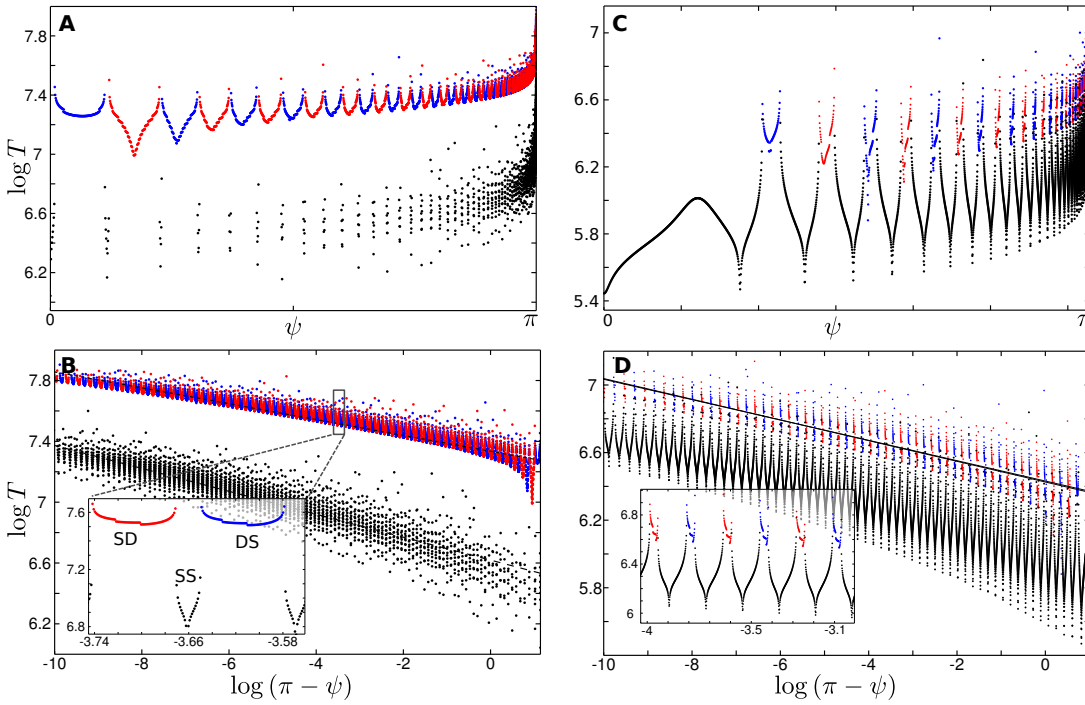


FIG. S2. Times to attractor. Parameter values for (A, B): $A = 0.1, \beta = 0.025$ at $\rho_1 = \rho_2 = 0.56625$ and for (C, D): $A = 0.1, \beta = 0.05$ at $\rho_1 = \rho_2 = 0.5$. Final destinations are color coded in red for SD, blue for DS and black for SS states.

- ii.) Test for convergence to limit point or limit cycle: $\|(\rho_1, \rho_2, \psi)|_{t=t_k} - (\rho_1, \rho_2, \psi)|_{t=t_{k+1}}\| < \epsilon_c$ with $\epsilon_c \sim 10^{-4}$
- iii.) Exit loop when a LP or LC is detected or 100 iterations are carried out.
- 3. If LC or LP is detected, the final state is detected as explained above. Otherwise, failed convergence is stored as a failed end state.

E. Destination maps in the s_c -plane

Destination maps were calculated for $\beta = 0.01, \dots, 0.125$ at constant $A = 0.2$ (Fig. S3A) and for $A = 0.08, \dots, 0.41$ at constant $\beta = 0.05$ (Fig. S3B). Saddle-node (SN) and homoclinic (HC) transitions are indicated.

F. Numerical continuation of the basin boundaries (separatrices)

The stable manifold of the saddle chimera defines the boundary of the basin of attraction of the corresponding stable chimera. By approximating this manifold, we can visualize which regions of the state space will evolve toward this chimera state, as shown in Fig. S4 and Fig. S5. The manifold can be approximated as follows:

Step 1: Compute the two stable eigenvectors of the saddle chimera to obtain a local approximation to the stable manifold near the saddle chimera. (There are two stable eigenvectors \mathbf{v}_1 and \mathbf{v}_2 and one unstable eigenvector \mathbf{v}_3 for the saddle chimera located at \mathbf{p} . The stable eigenvectors define a plane tangent to the stable manifold.)

Step 2: Obtain a family of starting points $\mathbf{x}_0(\theta)$ for continuation by making small perturbations off of the saddle chimera in every direction within the stable manifold. (Define a vector of angles θ and a magnitude ϵ . The family of starting points are defined by $\mathbf{x}_0(\theta) = \mathbf{p} + \epsilon [\cos(\theta)\mathbf{v}_1 + \sin(\theta)\mathbf{v}_2]$.)

In Fig. S4, we used 23 angles θ between 0 and π with the vectors \mathbf{v}_1 and \mathbf{v}_2 chosen so that all of these perturbations led to relevant parameter values and a perturbation magnitude of $\epsilon = 10^{-6}$. In Fig. S5, 94 trajectories were used.

Step 3: Integrate backward in time from each point until the trajectories reach \mathbf{x}_1 with a predetermined distance $\|\mathbf{x}_1 - \mathbf{x}_0\|$ from the start point, and plot the surface containing these trajectories. (We used `ode45` to integrate the equations and then interpolated to determine when the trajectories had reached the desired length.)

In Fig. S4, the predetermined distance was set at 0.01 to obtain a high resolution near the manifolds. In Fig. S5, the predetermined distance was set between 1 and 20 (and no additional refinement was performed) in order to reduce data points for quick

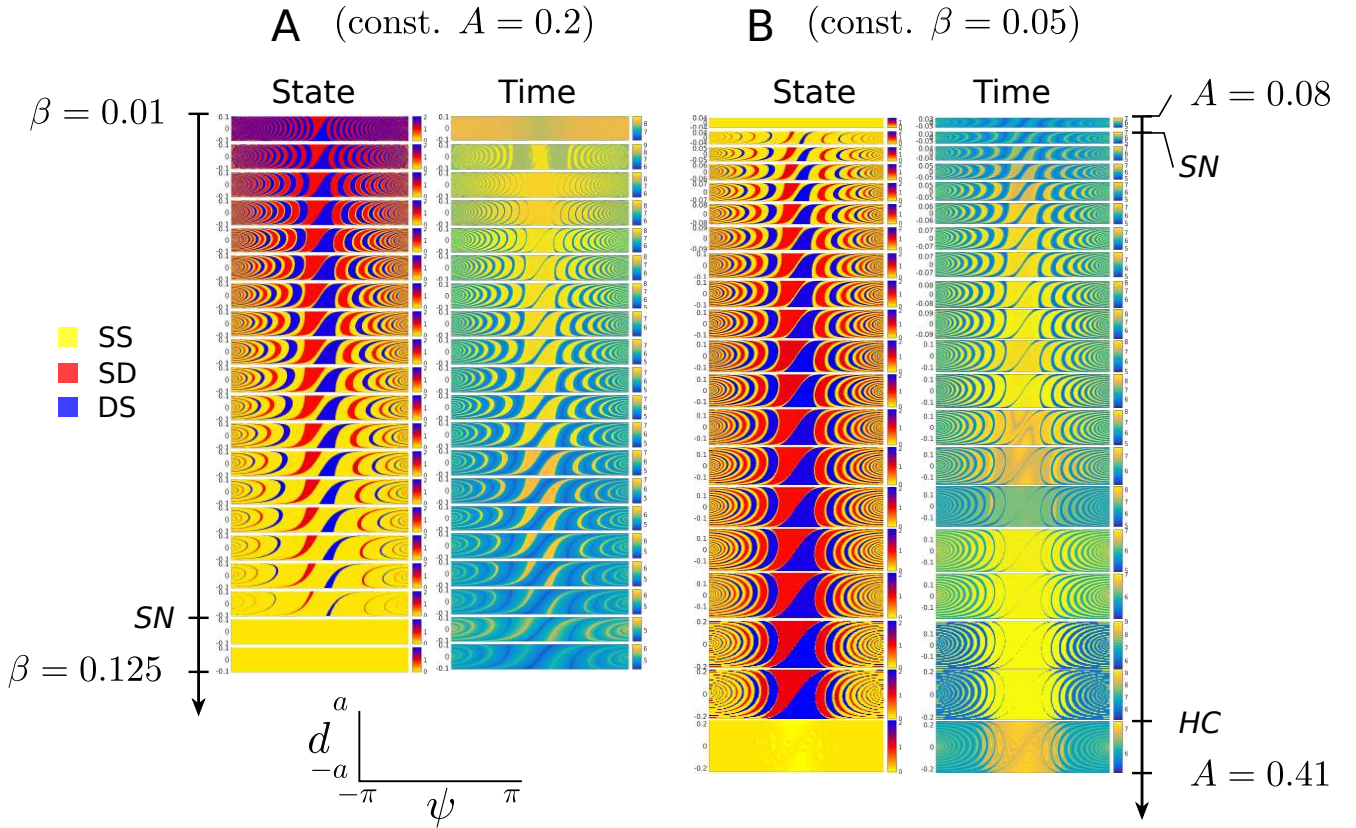


FIG. S3. Sweeps in parameter β (panel A), and in parameter A (panel B), showing destination map (left column) and logarithmic times to attractor (right column). The maps are shown in the (d, ψ) -plane at $s = s_c = 1 - A$. Parameters where saddle node and homoclinic bifurcations occur are denoted by SN and HC, respectively.

rendering, and in particular to enhance the visibility of the separatrices while reducing the total number of points displayed. This way the point families are equidistant in space, rendering an accurate picture of the separatrix surface in all regions.

Step 4: The endpoints of the trajectories define a curve. Use evenly spaced points along the curve as new starting points and return to step 3 until enough of the stable manifold has been computed.

In Fig. S4, we used a spacing of 0.01 near the saddle chimera and 0.05 once the trajectories had reached a distance of 0.2 from the saddle chimera.

V. PERTURBATION ANALYSIS AROUND THE INVARIANT RAYS R_0 AND R_π

A. Perturbation analysis near R_0 manifold

As discussed in the main text, we consider the coupling constants (μ, ν) to be perturbed from global coupling by setting $\mu = \frac{1}{2}(1 + A)$, $\nu = \frac{1}{2}(1 - A)$ as in [1]. We then make the perturbative approximation that ψ, d, β and A are all small and of the same order (while keeping in mind that $A > 2\beta$ is required for existence of a chimera state in this limit):

$$\begin{aligned} \psi &= \psi_1 \epsilon + \mathcal{O}(\epsilon^2), & d &= d_1 \epsilon + \mathcal{O}(\epsilon^2), \\ \beta &= \beta_1 \epsilon + \mathcal{O}(\epsilon^2), & A &= A_1 \epsilon + \mathcal{O}(\epsilon^2). \end{aligned}$$

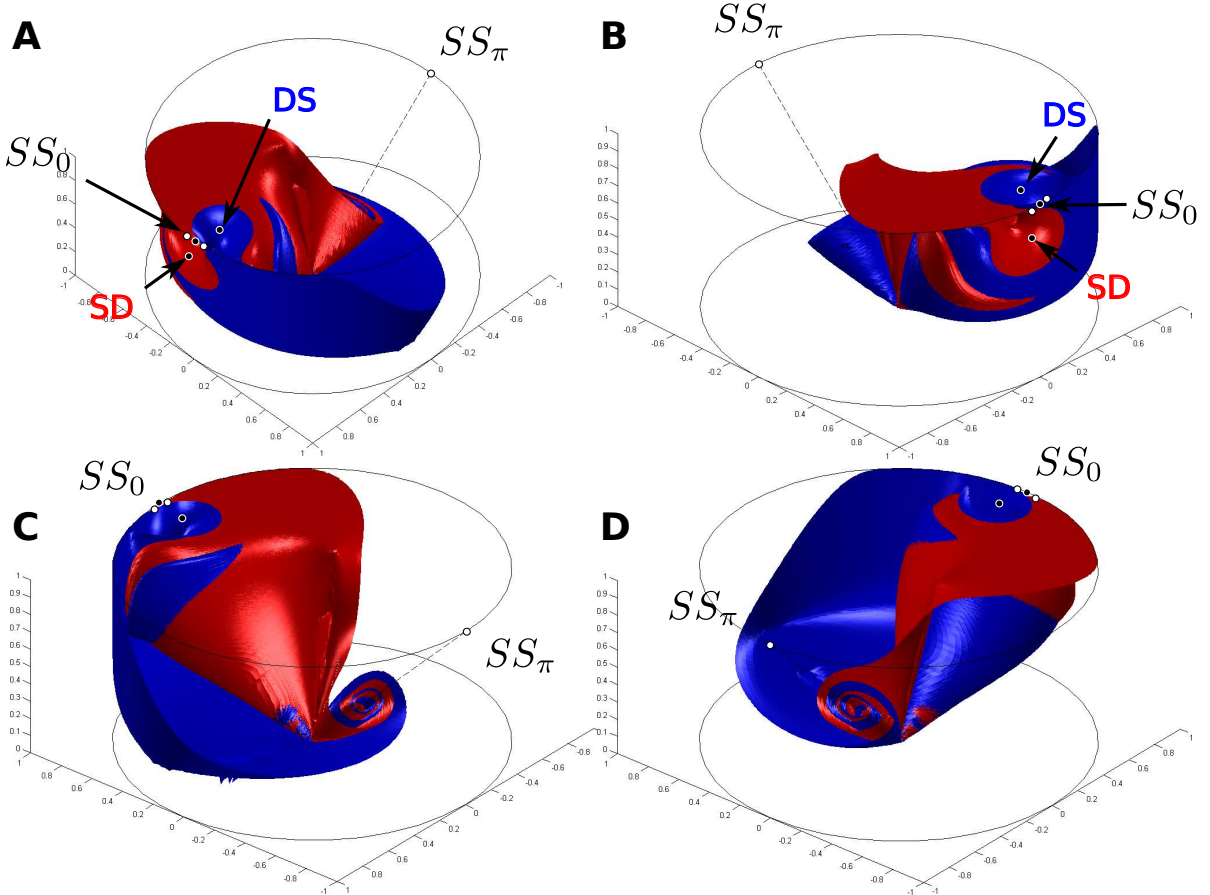


FIG. S4. Separatrix surfaces continued from the SD and DS saddle points on the S_1 (red) and S_2 (blue) manifolds, respectively, shown from different view angles **(A, B, C, D)**. Continuation is performed as described in the text for $A = 0.1$ and $\beta = 0.025$. Black and white dots denote stable and unstable fixed points, respectively.

After making a change of variables $x = d_1$, $y = \frac{1}{2}s\psi_1^1$, and then a second change of variables $x = r \cos(\theta)$ and $y = r \sin(\theta)$ we find the following equations:

$$\frac{dr}{dt} = - \left(\frac{1}{2}A_1 \sin(2\theta) + \beta_1 \right) s^2 r \epsilon, \quad (30)$$

$$\frac{d\theta}{dt} = \frac{1}{2} (1 - s^2) - \frac{1}{2} [1 + \cos(2\theta)s^2] A_1 \epsilon, \quad (31)$$

$$\frac{ds}{dt} = \frac{1}{2}s (1 - s^2) \beta_1 \epsilon. \quad (32)$$

Note that the derivatives of r and s are both order ϵ while the derivative of θ is order 1 (when s is not close to 1). Thus θ evolves on a fast time scale while r and s evolve slowly. We therefore use the method of averaging on the higher order terms involving θ to simplify these equations to

$$\frac{dr}{dt} = -\beta_1 s^2 r \epsilon, \quad (33)$$

$$\frac{d\theta}{dt} = \frac{1}{2} (1 - s^2 - A_1 \epsilon), \quad (34)$$

$$\frac{ds}{dt} = \frac{1}{2}s (1 - s^2) \beta_1 \epsilon. \quad (35)$$

¹ The change of variables is chosen so that that the spiraling cycles become circular in shape.

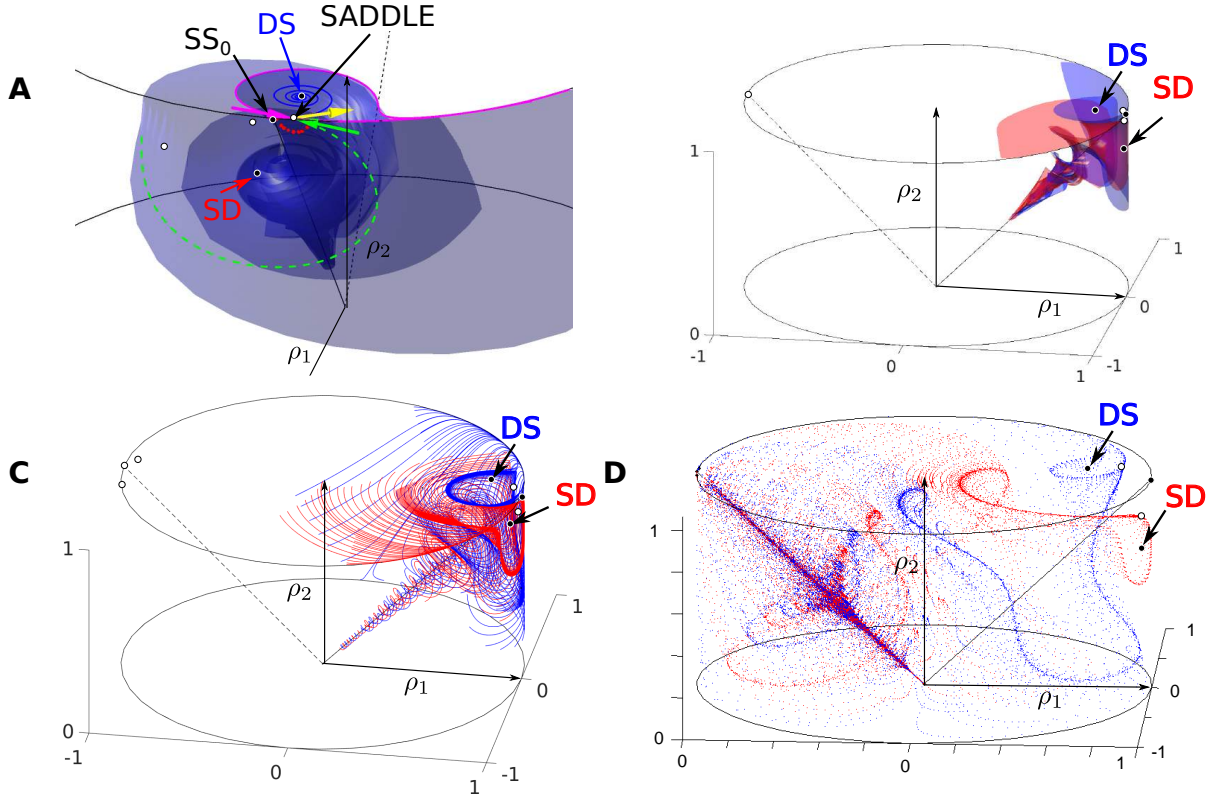


FIG. S5. Visualization of separatrix surfaces and trajectories. Points along the separatrix corresponding the DS chimera state are colored blue and points along the separatrix corresponding the SD chimera state are colored red. **A:** Continuation of the separatrix for the DS chimera state. Stable manifold and corresponding eigenvectors of SADDLE are shown solid (magenta) and dashed (green), and unstable eigenvector in yellow. Red dots indicate initial points from where the stable manifold (blue) was continued. **B:** Superposition of the two continued separatrix surfaces. The continuation in A and B is performed as described in the text. **C:** Trajectories along the separatrix surfaces originating from SD and DS saddles points on the S_1 and S_2 manifolds, respectively. **D:** Trajectories along the separatrix surfaces, continued from saddle chimeras. Parameters are $\beta = 0.025$ and $A = 0.1$ (**A-C**) or $A = 0.2$ (**D**).

This reveals a couple of properties. First of all, as expected, solutions will be spirals around the R_0 manifold. The radius r goes to 0 as $t \rightarrow \infty$ (for the truncated equations). Thus, trajectories slowly converge toward the manifold until the approximations break down when $\frac{d\theta}{dt} = 0$ and higher order terms become significant. The frequency of rotation is $\omega = \frac{1}{2}(1 - s^2 - A_1\epsilon)$. So, when $s = \sqrt{1 - A}$, the frequency is 0. In the main text, this is referred to as the s_c -plane. In this plane, the trajectories begin to separate and evolve toward the fully synchronized state or the DS or SD chimeras.

Note that there is an alternative way that the “critical plane” could be defined. Setting $d\theta/dt = 0$ in Eq. (31) yields a minimum s solution $s_c = 1 - A_1\epsilon + \mathcal{O}(\epsilon^2)$ (possible only for particular θ values), thus $s_c \approx 1 - A$ is the smallest value of s for which rotation about ray R_0 may stop.

The difference between the two expressions $s_c \approx \sqrt{1 - A} \approx 1 - A/2$ and $s_c \approx 1 - A$ comes from whether averaging has been applied or not. In the former case (averaged equations), rotation about R_0 stops on average over all θ ; in the latter case, rotation about R_0 stops only for *some particular* θ .

Equation (35) can be solved explicitly to get

$$s(t) = s_0 / \sqrt{s_0^2 + (1 - s_0^2)e^{-\epsilon\beta_1 t}}.$$

Taking $\dot{\theta} = (1 - s^2)/2$ to lowest order (from (34)), we can substitute in for $s(t)$ and then integrate from $t = 0$ to $t = t_{\text{crit}}$ to approximate the total angle change about the R_0 manifold over the course of the trajectory. Here t_{crit} represents the time at which the trajectory $s(t)$ reaches the critical plane $s = s_c$:

$$t_{\text{crit}} = \frac{1}{\epsilon\beta_1} \ln \left(\frac{1 - s_0^2}{s_0^2} \frac{(2 - A)^2}{A(4 - A)} \right) = \frac{1}{\epsilon\beta_1} \ln \left(\frac{(1 - s_0^2)s_c^2}{(1 - s_c^2)s_0^2} \right).$$

Integrating $\dot{\theta}$ gives a total angle change

$$\Delta\theta = \frac{1}{\epsilon\beta_1} \ln \left(\frac{1 - A/2}{s_0} \right) = \beta^{-1} \ln(1 - A/2) - \beta^{-1} \ln s_0.$$

This can also be written as $\Delta\theta = \beta^{-1} \ln(s_c/s_0)$, and then, this expression is valid for either definition of s_c .

Since the angle of a trajectory at the critical plane determines the basin the trajectory belongs to, the appearance of the basin boundary in a section plane orthogonal to the ray R_0 is just a line with angle proportional to $\Delta\theta$.

B. Perturbation analysis near R_π manifold

We can perform a similar analysis near $\psi = \pi$.

$$\begin{aligned} \psi &= \pi + \psi_1 \epsilon + \mathcal{O}(\epsilon^2), & d &= d_1 \epsilon + \mathcal{O}(\epsilon^2), \\ \beta &= \beta_1 \epsilon + \mathcal{O}(\epsilon^2), & A &= A_1 \epsilon + \mathcal{O}(\epsilon^2). \end{aligned}$$

This time we make a change of variables $x = d_1$, $y = \frac{1}{2} \frac{s\sqrt{1-s^4}}{1+s^2} \psi_1^2$ ², and again convert to polar coordinates. This yields

$$\frac{dr}{dt} = \left[\frac{1}{2} \beta_1 (1 - s^2 \cos(2\theta)) - \frac{1}{2} s^2 \sqrt{\frac{1-s^2}{1+s^2}} \sin(2\theta) \right] r\epsilon \quad (36)$$

$$\begin{aligned} \frac{d\theta}{dt} &= -\frac{1}{2} \sqrt{1-s^4} \\ &+ \left[\frac{1}{2} \sqrt{\frac{1-s^2}{1+s^2}} (1 - s^2 \cos(2\theta)) A_1 + \frac{1}{2} \beta_1 \sin(2\theta) s^2 \right] \epsilon, \end{aligned} \quad (37)$$

$$\frac{ds}{dt} = \left[\frac{1}{2} s (1 - s^2) \beta_1 A_1 + \frac{1+s^2}{4s} \sqrt{\frac{1+s^2}{1-s^2}} r^2 \sin(2\theta) \right] \epsilon^2. \quad (38)$$

Again we find that the derivative of θ is larger than the other derivatives, allowing us to reduce the system to

$$\frac{dr}{dt} = \frac{1}{2} \beta_1 r \epsilon, \quad (39)$$

$$\frac{d\theta}{dt} = -\frac{1}{2} \sqrt{1-s^4} + \left[\frac{1}{2} \sqrt{\frac{1-s^2}{1+s^2}} A_1 \right] \epsilon, \quad (40)$$

$$\frac{ds}{dt} = \left[\frac{1}{2} s (1 - s^2) \beta_1 A_1 \right] \epsilon^2. \quad (41)$$

Similar to the results near R_0 , here we find that trajectories spiral around the R_π manifold. However, in this case, three distinct time scales are present and the radius diverges rather than converging. So rotation around the manifold occurs at a faster rate than divergence away, and both occur faster than translation along the manifold.

C. Shape of the basin boundaries

We can understand two qualitative aspects of basin boundaries seen in numerics: (1) the basin boundary between the SD and DS chimeras is linear in the s_c -plane near R_0 , and (2) the basin boundary has a spiral shape near R_π .

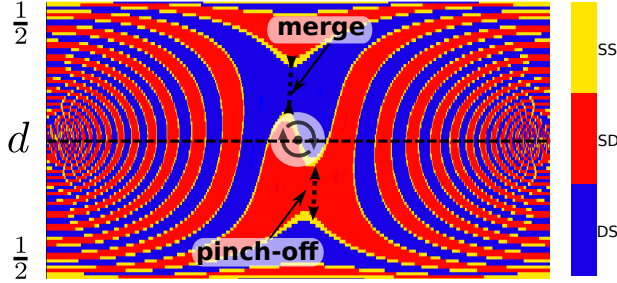
To understand the shape near R_0 , it is helpful to consider trajectories generated by points along a straight line orthogonal to R_0 . Consider the set of points along a line segment parameterized by k where $r = kr_0$, $\theta = \theta_0$ and $s = s_c$ for $-1 \leq k \leq 1$. The trajectories generated by integrating the equations with initial conditions along that line segment will intersect the plane perpendicular to R_0 at some later time at $s = s_c + \delta$ where $\delta \ll \epsilon$. By symmetry, if a point along the line with $k > 0$ evolves toward the DS chimera, then the corresponding point with $k < 0$ will be mapped to the SD chimera. Similarly, if a point with $k > 0$ is mapped to the synchronized state, the corresponding point with $k < 0$ will also be mapped to the synchronized state.

² The change of variables is chosen so that the spiraling cycles become circular in shape; the particular shape differs from the one near the R_0 -manifold.

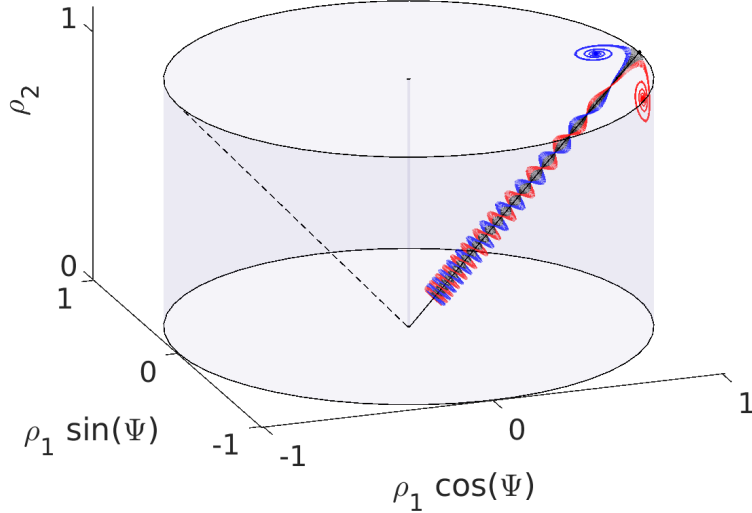
Suppose $r_0 \ll \delta$, so that all points along the line segment are chosen to be arbitrarily close to the R_0 manifold. According to Eqs. (30)-(32), $d\theta$ is independent of r , so the images of these points in the plane $s_c + \delta$ will remain collinear. Now $dr = \mathcal{O}(\delta^2)$ and $ds = \delta$, so not only will the points along this segment remain collinear, they will also remain arbitrarily close to each other and to R_0 as s increases. For at least one particular choice of θ_0 , this line segment will reach the surface of the cylinder in a direction tangent to the intersection of the invariant surfaces S_1 and S_2 . As discussed above, this intersection is itself an invariant manifold, and thus the entire line segment will be mapped to the synchronized state. This particular line segment, which originates from a line segment in the s_c plane, therefore represents a separatrix between SD and DS chimeras³.

Near R_π the picture is different. Because there are three distinct time scales, with the evolution of both θ and r faster than the evolution of s , trajectories initially close to R_π look like spirals within a fixed plane perpendicular to s —this is the origin of the spiral shape of the separatrix structure near R_π .

D. Supplementary Videos

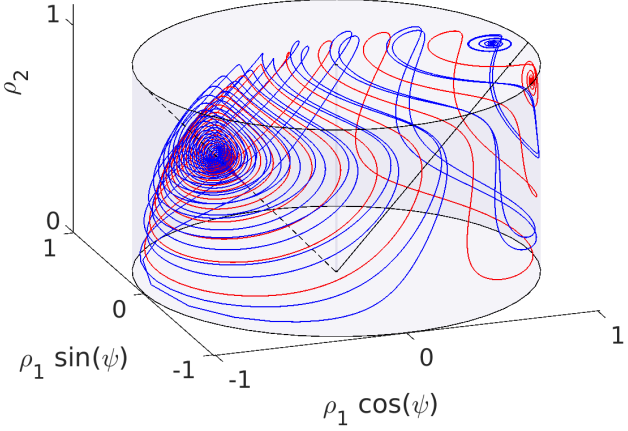


Video 1. Destination maps as a function of $0.1 \leq s \leq 1$ ($A = 0.2, \beta = 0.025$). Even though $A = 0.2$ is fairly large with regards to our perturbative calculus, numerical results match the predicted motion qualitatively well. As s increases from zero, basins merge and pinch-off in an alternating fashion, so that the basin boundaries rotate counter-clockwise about R_0 ($(d, \psi) = (0, 0)$). Once s reaches $s_c \approx \sqrt{1 - A}$, this rotation stops, demonstrating that knowledge of the trajectory position in the $s = s_c$ plane is sufficient for determining the final fate of the trajectory. To watch video, look for Ancillary Files on arXiv or see http://eam.webhop.net/mov/SI_Video1_BOA.mp4.

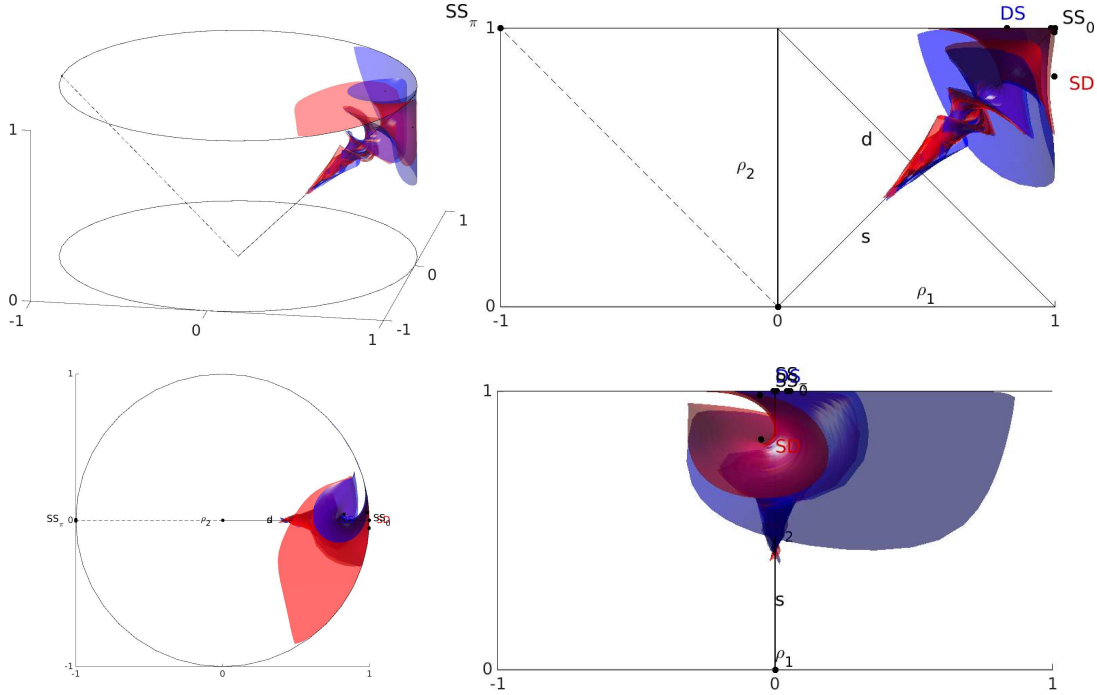


Video 2. Twisting motion of trajectories in a double helical structure following the R_0 -manifold ($A = 0.1, \beta = 0.025$). Initial conditions of 31 trajectories are equally spaced with $s = 0.1045, -0.0345 \leq d \leq 0.0345, \psi = 0$. To watch video, look for Ancillary Files on arXiv or see http://eam.webhop.net/mov/SI_Video2_BOA.mp4.

³ This qualitative argument can be made rigorous in the limit where the SS_0 basin becomes a set of measure zero (infinitesimal thickness), and gives useful insight in other cases.



Video 3. Twisting motion of trajectories in a double helical structure following the R_π manifold ($A = 0.1, \beta = 0.025$). Initial conditions of the 3 trajectories are $s = 0.4487, d \in \{-0.6, -0.2, 0.6\} \times 10^{-3}, \psi = \pi$. To watch video, look for Ancillary Files on arXiv or see http://eam.webhop.net/mov/SI_Video3_BOA.mp4.



Video 4. Three dimensional visualization of the separatrices emanating from the chimera saddle points near the R_0 -manifold ($A = 0.1, \beta = 0.025$). To watch video, look for Ancillary Files on arXiv or see http://eam.webhop.net/mov/SI_Video4_BOA.mp4.

[1] D. M. Abrams, R. E. Mirollo, S. H. Strogatz, and D. A. Wiley, *Phys. Rev. Lett.* **101**, 084103 (2008); E. Montbrió, J. Kurths, and B. Blasius, *Phys. Rev. E* **70**, 056125 (2004); E. A. Martens, *Chaos* (Woodbury, N.Y.) **20**, 043122 (2010).

[2] E. Ott and T. M. Antonsen, *Chaos* (Woodbury, N.Y.) **18**, 037113 (2008); *Chaos* **023117** (2009); E. Ott, B. R. Hunt, and T. M. Antonsen, *Chaos* (Woodbury, N.Y.) **21**, 025112 (2011).

[3] M. J. Panaggio and D. M. Abrams, *Nonlinearity* **28**, R67 (2015).

[4] S. Watanabe and S. H. Strogatz, *Physica D* **74**, 197 (1994).

[5] A. Pikovsky and M. Rosenblum, *Phys. Rev. Lett.* **264103**, 1 (2008).

[6] C. R. Laing, *Chaos* (Woodbury, N.Y.) **19**, 013113 (2009).

[7] C. R. Laing, *Chaos* (Woodbury, N.Y.) **22**, 043104 (2012).